Classification:
Biophysics and computational biology; Evolution

Title:

Biophysical principles of choanoflagellate self-organization

Authors:

Ben T. Larson[1,2], Teresa Ruiz-Herrero[3], Stacey Lee[4], Sanjay Kumar[4,5], L. Mahadevan[3,6]*, Nicole King[1]*

Affiliations:

[1]Howard Hughes Medical Institute and the Department of Molecular and Cell Biology, University of California, Berkeley, CA, USA

[2]Biophysics Graduate Group, University of California, Berkeley, CA, USA

[3]Paulson School of Engineering and Applied Sciences, Harvard University, Cambridge, MA, USA

[4]UC Berkeley-UCSF Graduate Program in Bioengineering, Department of Bioengineering, University of California, Berkeley, CA, USA

[5]Department of Chemical and Biomolecular Engineering, University of California, Berkeley, CA, USA

[6]Departments of Physics and Organismic and Evolutionary Biology, and Kavli Institute for NanoBio Science and Technology, Harvard University, Cambridge, MA, USA

*Corresponding author. Email: nking@berkeley.edu and lmahadev@g.harvard.edu

Keywords:

morphogenesis, multicellularity, quantitative microscopy, physical constraints, extracellular matrix, morphospace

Abstract

Inspired by the patterns of multicellularity in choanoflagellates, the closest living relatives of animals, we quantify the biophysical processes underlying the morphogenesis of rosette colonies in the choanoflagellate *Salpingoeca rosetta*. We find that rosettes reproducibly transition from an early stage of 2D growth to a later stage of 3D growth, despite the underlying stochasticity of the cell lineages. We postulate that the extracellular matrix (ECM) exerts a physical constraint on the packing of proliferating cells, thereby sculpting rosette morphogenesis. Our perturbative experiments coupled with biophysical simulations demonstrates the fundamental importance of a basally-secreted ECM for rosette morphogenesis. In addition, this yields a morphospace for the shapes of these multicellular colonies, consistent with observations of a range of choanoflagellates. Overall, our biophysical perspective on rosette development complements previous genetic perspectives and thus helps illuminate the interplay between cell biology and physics in regulating morphogenesis.

Significance statement

Comparisons among animals and their closest living relatives, the choanoflagellates, have begun to shed light on the origin of animal multicellularity and development. Here we complement previous genetic perspectives on this process by focusing on the biophysical principles underlying colony morphology and morphogenesis. Our study reveals the crucial role of the extracellular matrix in shaping the colonies and leads to a phase diagram that delineates the range of morphologies as a function of the biophysical mechanisms at play.

Introduction

Nearly all animals start life as a single cell (the zygote) that, through cell division, cell differentiation, and morphogenesis, gives rise to a complex multicellular adult form (1, 2). These processes in animals require regulated interplay between active cellular processes and physical constraints (3–9). A particularly interesting system in which to study this interplay is the choanoflagellates, the closest relatives of animals (10–12). Choanoflagellates are aquatic microbial eukaryotes whose cells bear a diagnostic "collar complex" composed of an apical flagellum surrounded by an actin-filled collar of microvilli (13, 14) (Fig. 1). The life histories of many choanoflagellates involve transient differentiation into diverse cell types and morphologies (15, 16). For example, in the model choanoflagellate *Salpingoeca rosetta*, solitary cells develop into multicellular colonies through serial rounds of cell division (17), akin to the process by which animal embryos develop from a zygote (Fig. 1A). Therefore, choanoflagellate colony morphogenesis presents a simple, phylogenetically-relevant system for investigating multicellular morphogenesis from both a biological and a physical perspective (14).

S. rosetta forms planktonic rosette-shaped colonies ("rosettes"), in which the cells are tightly packed into a rough sphere that resembles a morula-stage animal embryo (17). Because the cell division furrow forms along the apical-basal axis, thereby dissecting the collar, all of the cells in rosettes are oriented with their flagella and collars facing out into the environment and their basal poles facing into the rosette interior (Fig. 1B). Interestingly, all three genes known to be required for

rosette development are regulators of the extracellular matrix (ECM): a C-type lectin called *rosetteless* (18) and two predicted glycosyltransferases called *jumble* and *couscous* (19). Nonetheless, little is known about either the mechanistic role of the ECM or the extent to which rosette morphogenesis is shaped by physical constraints.

A critical barrier to understanding the biological and physical mechanisms underlying rosette morphogenesis has been the absence of a detailed characterization of the morphogenetic process. For example, it is not known whether rosettes form through the development of invariant cell lineages akin to those seen in *C. elegans* (20) or through stochastic cell divisions, as occurs, for example, in sponges and mice (21, 22). Moreover, it is not known whether there are identifiable developmental stages in rosette development. To quantify the principles of rosette morphogenesis, we used a combination of quantitative descriptions of rosette development, experimental perturbations, and biophysical simulations that together reveal the importance of the regulated secretion of basal ECM in physically constraining proliferating cells and thereby sculpting choanoflagellate multicellularity.

Results

Rosette morphogenesis displays a stereotyped transition from 2D to 3D growth

To constrain our search for mechanistic principles, we first quantified the range of sizes and spectrum of morphologies of *S. rosetta* rosettes by measuring the population-wide distribution of rosette size in terms of cell number. *S. rosetta* cultured solely in the presence of the rosette-inducing bacterium *A. machipongonensis* (23), lead to a population with a stationary cell number distribution. While some rosettes contained as many as 25 cells, the most common rosette size was 8 cells/rosette, with 51% of rosettes containing between 6-8 cells (Fig. 2A). While rosettes grow through cell division, their ultimate size is determined by either colony fission (as previously reported; 16) or cell extrusion (Fig S1). In each case, the rosettes contained 8 or more cells, suggesting that these rosette size decreasing phenomena are more common in larger rosettes.

We next quantified defining features of the 3D morphology of rosettes containing between four (following (24), we defined four cells as the smallest cell number clearly identifiable as a rosette) to twelve cells (representing 90% of rosettes at steady state, Methods; Fig. 2B, C). This analysis revealed that rosettes increased in volume and diameter as cell number increased (Fig. 2D). Although the average cell volume reduced between the four-cell and five-cell stages of rosette development, average cell volume did not change substantially with increasing cell number after the five-cell stage (Fig. S2), suggesting that cells in rosettes grow between cell divisions. This contrasts with cleavage in the earliest stages of animal

115 embryogenesis, in which cell volume steadily decreases as cell divisions proceed
116 with no cell or overall tissue growth (2).

117 Our analyses revealed that rosette morphogenesis displays two distinct, but
118 previously undescribed phases: (1) a 2D phase of growth from four to seven cells,
119 during which the overall shape of rosettes changed substantially with increasing cell
120 number and (2) a 3D phase from eight to twelve cells, during which rosettes
121 expanded nearly isotropically (Fig. 2C-E). Interestingly, the most common rosette
122 size (8 cells) corresponded to the transition between the two phases of growth.

123 Transitions from 2D to 3D growth can be driven by the constrained growth
124 of cell layers leading to increasing mechanical stresses (25–29). We hypothesized
125 that the physical packing of cells in rosettes might constrain cell growth and
126 proliferation and help explain the growth transition during rosette morphogenesis.
127 Indeed, cell packing initially increased (as indicated by an increase in the number of
128 nearest neighbor cells, Fig. 2F, and suggested by the reduced average sphericity of
129 cells, Fig. S2). Following the growth transition at the 8-cell stage, cell packing
130 continued to increase with increasing cells/rosette, although the rate of increase
131 slowed as a function of the number of cells/rosette (Fig. 2F). Therefore, the
132 transition to isotropic 3D growth in eight-cell rosettes may occur in response to the
133 accumulation of stress caused by the increase in cell packing in growing rosettes.
134

135 ***Rosette developmental dynamics are stochastic***

136 The influence of cell packing on rosette morphogenesis did not preclude the
137 possibility that the rosette developmental program might also involve specific

patterns of cell division that result in well-defined cell lineages. We therefore documented cell lineages in live, developing rosettes (Fig. 3). Consistent with the single previous published observation of live rosette development (17), the cells maintained polarity throughout development, with their division planes oriented along the apical-basal axis. Relative to the cell division times in linear chains (Fig. 1A), which form when rosette inducing bacteria are absent, we observed a slight but statistically significant increase in division rate in rosettes ($p=0.03$ by Wilcoxon rank sum test Fig. S3). In addition, we found that both the order and timing of cell divisions differed among different rosettes (Fig. 3B, C), ruling out the possibility that cell lineages are invariant. This process of apparently unpatterned cell divisions resembles the dynamics of early embryogenesis in diverse animals, including sponges and mice (21, 22).

Although division patterns were variable between rosettes, ruling out the possibility of invariant cell lineages, in no rosette did cells from the first, second, or third cell division give rise to more than 60% of cells (Fig. 3D). Moreover, cell division remained balanced throughout rosette morphogenesis, with no cell lineage coming to dominate. Importantly, the cell lineages of chains showed the same kind of stochasticity and variability as rosettes (Fig. 3D). These observations suggest that rosette morphogenesis does not require the strongest forms of cell cycle control or coordination (i.e. the synchronous divisions or deterministic division timing or order observed in the development of some animals such as *C. elegans*, *Xenopus, Drosophila,* and zebrafish (30–33) and in the green alga *Volvox* (34–36)).

ECM constrains proliferating cells in rosettes

To reconcile the stereotyped 3D growth transition (Fig. 2) with the stochastic developmental dynamics of rosette formation (Fig. 3), we set out to test the "ECM constraint hypothesis (Fig 4A, B)." This hypothesis was motivated by the idea that physical constraints imposed by the geometry and mechanics of cell packing play a key role in morphogenesis and that the source of the physical constraint in growing rosettes is the ECM, which is known to be required for rosette morphogenesis and connects all cells in a rosette, filling the rosette center (16, 18, 19, 37). The phenomenon of physically constrained morphogenesis suggests that the amount of ECM secreted during rosette development is an important factor in sculpting rosette morphogenesis (Fig. 4A, B). We visualized and quantified the volume of the ECM by staining with fluorescein-conjugated Jacalin, a galactose-binding lectin (19, 38). Importantly, Jacalin does not stain chains, so its target is likely specific to rosette ECM (19). We found that the relative amount of space occupied by basal ECM (ECM volume/total cell volume, denoted by ϕ) in developing rosettes was constant and maintained at roughly 6% (Fig. 4C). Therefore, we infer that cells in rosettes produce ECM at a constant rate relative to the growth of cells, either through synthesis and secretion alone or through a balance of regulated synthesis, secretion, and degradation.

A key prediction of the ECM constraint hypothesis (Fig. 4A, B) is that compressive stress on cells, balanced by stress in the ECM, should increase with cell number. Alternatively, cell-cell connections mediated by lateral cell-cell adhesion or cytoplasmic bridges formed during incomplete cytokinesis (16, 37) (Fig. 1B) might

be primarily responsible for the structural integrity of rosettes. If cell-cell connections dominate over ECM in holding together rosettes, we would expect cells to be under tension such that measured stresses would be in the opposite direction to those predicted by the ECM constraint hypothesis.

To probe the balance of forces in developing rosettes, we performed laser ablation experiments, which provided a readout of the relative magnitude and direction of stresses within rosettes (39–42). Upon ablation of a single cell in a rosette, we found that the remaining cells immediately became more rounded and moved closer together, reducing the size of the gap left by the ablated cell (Fig. 4E. This result demonstrated that residual elastic stress (as measured by initial recoil velocity after ablation, (39)) is maintained in rosettes, with cells under compressive stress balanced by an additional component of residual stress. If rosettes were primarily held together by strong cell-cell adhesion or constrained by cytoplasmic bridges (Fig. 1B), the expected recoil would have been in the opposite direction, causing a larger gap to open in rosettes, due to cells increasing contact area with remaining neighbors in the former case and tension in bridges in the latter. Moreover, as the number of cells in rosettes increased, the measured residual stress increased (Fig. 4F), consistent with the ECM constraint hypothesis (Fig. 4A, B). These results ruled out strong cell-cell adhesion or constraint by cytoplasmic bridges as the dominant physical mechanisms underlying rosette integrity and morphogenesis.

Additionally, residual stress (as measured by initial recoil velocity (7, 39, 43)) displayed a sharp increase, by nearly a factor of two, at the 8-cell stage (Fig.

4F), coinciding with the 3D growth transition (Fig. 2). In conjunction with the observed increase in cell packing (Fig. 2F), this result suggested that the packing of cells is mechanically constrained in developing rosettes such that cells are increasingly compressed against one another with increasing cell number. We reasoned that the shared ECM secreted from the basal end of cells, adhesion to which is likely essential for rosette formation (18, 19), might be the source of this constraint. While we have ruled out bridges as a dominant component of the structural integrity of rosettes, they could play a role in stabilizing cell orientation to hinder out of plane growth during the 2D phase of rosette morphogenesis.

Material properties of ECM affect morphogenesis

We next sought to test the ECM constraint hypothesis through perturbative experiments. While the hypothesis entails that changing geometrical properties such as cell shape and relative amount of ECM should have a substantial effect on rosette morphogenesis, these properties could not be experimentally tuned. However, we could perturb the mechanical properties of the ECM. To do so, we treated developing rosettes with strontium chloride ($SrCl_2$). Strontium is a divalent cation that can stiffen hydrogels, including animal ECM, by increasing crosslinking density (44–48). Importantly, we found that $SrCl_2$ has no detectable effect on cell growth at up to twice the highest concentration used during this set of experiments (Fig. S4). Under our ECM constraint hypothesis, we predicted that increased ECM stiffness would alter morphogenesis by further constraining cell packing, thus holding cells in a more compact arrangement along with a relative increase in

residual stress. Consistent with our hypothesis, we found that rosettes became more compact with increasing $SrCl_2$ concentration (Fig. 5A, B), and the 3D transition shifted to lower cell numbers, occurring at the five-cell stage for the highest $SrCl_2$ concentration (Fig. 5C). Additionally, the transition to isotropic growth at the 8-cell stage was abolished (Fig. 5B). Together, these analyses reveal that morphogenesis is altered.

Using laser ablation experiments, we found that relative residual stress as determined by maximum initial recoil velocity (as in Fig. 4E, F) was significantly increased for $SrCl_2$-treated 4-7 cell rosettes relative to untreated rosettes (Fig. 5D). The increase in residual stress in conjunction with the 2D to 3D growth transition at lower cell numbers, supported the hypothesis that ECM-constrained proliferation is a key driver of the 3D transition in rosette morphogenesis. Interestingly, for the 8-cell-stage and higher, we did not find a significant increase in residual stress in $SrCl_2$-treated rosettes compared to untreated rosettes. This is consistent with cells exerting maximum growth pressure on their neighbors at the 8-cell stage and above. Taken together, these results confirm important model predictions by demonstrating that material properties of the ECM can affect morphogenesis, which highlights the central role of the ECM in sculpting rosette morphology.

Amount of ECM, cell shape, and ECM stiffness as control parameters for morphogenesis

To formalize and test our hypothesis of morphogenesis shaped by ECM constraint (Fig. 4A, B), we next developed a cell-based computational model to

simulate rosette development. Because development involves few cells (ruling out continuum modeling) in a low Reynolds number environment where inertial forces play a negligible role (49, 50) we developed particle-based simulations akin to Brownian dynamics, but neglected the role of thermal fluctuations given the large size of the cells and aggregates (51). In the model, the ECM and cells were represented by a system of interacting spherical particles (Fig. 6A). This particle representation also allowed us to capture the discrete and stochastic nature of cell division and the stochastic nature ECM secretion as well the polarity of cell division and ECM secretion. Each cell in the model was composed of three linked spheres to capture cell shape and for computational tractability, with a small sphere representing the basal pole of the cell, a larger sphere representing the cell body, and the largest representing the collar exclusion region. Cells interacted sterically with one another. The ECM was modelled as a system of small spheres with attractive interactions in order to capture the complex shapes the ECM can take on (Fig 4C) as well as its deformability. ECM particles similarly shared attractive interactions with the basal poles of cells. Cells in the model were allowed to divide stochastically, with the division plane orientation around the apico-basal axis determined by the previous division (consistent with observations of rosette development from Fig. 3 and (17)), and ECM particles were secreted stochastically at a constant rate from the basal pole of non-dividing cells (see Methods for a more detailed description of the model and simulations).

In this simplified model of rosette morphogenesis, three main parameters characterized the system: cell aspect ratio (length along apical/basal axis vs.

276 equatorial diameter), α, amount of ECM relative to total cell volume, ϕ, and relative
277 stiffness of the ECM (in terms of the strength of ECM-ECM adhesion bonds relative
278 to the force exerted by growing and dividing cells), σ. Simulations with parameter
279 values constrained by cell and ECM morphology data collected as part of this study
280 showed that this simple model was sufficient to recapitulate rosette morphogenesis,
281 including the expected 3D transition at the 8-cell stage (Fig. S5). Furthermore,
282 simulations showed that rosette morphogenesis was robust to a range of scaled
283 ECM stiffness values (Fig. 6B-E, S5) and to the stochasticity of cell divisions (Fig. S5).
284 We did find that simulations fail to recapitulate all aspects of rosette
285 morphogenesis, most saliently, the growth scaling (Fig. 2D) and the absolute
286 magnitudes of flatness and sphericity (Fig. 2E, S5). We expect, however, that a more
287 detailed treatment of the mechanics of cells and ECM may capture these aspects of
288 rosette morphogenesis more accurately, but such a detailed model is beyond the
289 scope of the present study.

290 Exploration of the effects of different parameter values revealed that the
291 model captures a range of different colonial morphologies (Fig. 6B, F). This space of
292 forms and associated model parameters constitutes a theoretical morphospace (51)
293 of ECM-based colonial choanoflagellate morphologies given this simplified model of
294 morphogenesis. Interestingly, some of the simulated forms resembled colonies, such
295 as tree-like structures (found in *Codosiga cymosa* (52) and an uncharacterized
296 *Salpingoeca sp.*, Fig. 6Gt_2, t_3) or cups (found in *Codosiga umbellata* (53) and another
297 uncharacterized *Salpingoeca sp.*, Fig. 6Gc_4, c_5), that have been previously reported in
298 other choanoflagellate species (Fig. 6F, G). We found that colony morphogenesis is

299 particularly sensitive to α and ϕ, changes in each of which can lead to dramatic
300 changes in predicted multicellular forms. For example, holding the other two
301 parameters fixed, increase in ϕ alone would be predicted to drive a change from
302 rosettes to disks or cups and from cones to trees (Fig. 6C, D). Colony morphogenesis
303 was also affected by changes in σ, but the effects tended to be subtler, such as
304 changes in cell packing over a relatively wide range of values (Fig. S5). In contrast
305 with changes in ϕ, increase in σ alone was either not predicted to lead to any
306 transitions in predicted colony morphology type or, at most, lead to single
307 transitions such as from rosettes to disks (Fig. 6D, E). These results demonstrate
308 that basal secretion of a shared ECM constitutes a robust yet flexible mechanism for
309 regulating multicellular morphogenesis. Furthermore, these results made specific
310 predictions about different colony morphologies corresponding to specific cell
311 morphologies and relative ECM volumes and stiffnesses.
312

Discussion

Our quantitative analyses, experimental perturbations, and simulations allowed us to understand the process by which single cells of *S. rosetta* gives rise to multicellular rosettes. We found that the earliest stages of rosette morphogenesis proceed through 2D anisotropic growth, which is stereotypically followed by a transition to 3D isotropic growth. In particular, we found that the basal ECM secreted by cells during rosette development physically constrains proliferating cells, and thereby drives a stereotyped morphogenetic progression in the absence of strict cell lineage specification and division timing. Simulations showed that this simple mechanism, the regulated basal secretion of ECM, is sufficient to not only recapitulate rosette morphogenesis but yield a morphospace that can not only explain the multicellular morphology of *S. rosetta* but also that of other species of colonial choanoflagellates. These results emphasize the importance of the choanoflagellate ECM for morphogenesis and should encourage future studies of its composition, physical properties, and regulation.

The importance of the basal ECM revealed in this study may generalize to other choanoflagellate species and colonial morphologies. Our simulations predict that differences in ECM levels (resulting from differing rates of biosynthesis, secretion, or degradation), cell shape, and in ECM stiffness relative to cells are sufficient to explain the existence of radically different colony morphologies across diverse choanoflagellates. Measurements and comparisons of ECM levels (ϕ), cell shape (α), and ECM stiffness (σ), in diverse colonial choanoflagellates will be crucial

to validate the model, and deviations from the predictions of the model could point to additional regulatory mechanisms.

From a broader perspective, rosette morphogenesis shows interesting parallels to mechanisms underlying morphogenesis in diverse other taxa. In terms of physical mechanisms, the constrained proliferation of cells that occurs during rosette development generates crowding stresses like those that regulate morphogenesis by animal epithelia (54, 55), snowflake yeast (56), and bacterial biofilms (26). In epithelia, compaction of cells due to crowding has been proposed as a general signal for cellular processes underlying tissue homeostasis such as apoptosis and extrusion (57–60). Further, accumulation of stress due to crowding of cells produces a jamming-like behavior that has been proposed as a generic constraint on the development of multicellular systems with fixed cell geometry (56). Due to the generality of physical constraints on cell packing, it is plausible that such phenomena acted both as constraints and regulatory mechanisms in the development and morphogenesis of early animals and their ancestors.

Cellular mechanisms of rosette morphogenesis are also shared with other multicellular systems. Our results demonstrate that the regulation of basal ECM sculpts the multicellular morphology of rosettes. Thus, our biophysical studies have converged on results from genetic screens in *S. rosetta* that implicated animal ECM gene homologs in the regulation of rosette development, including a C-type lectin (18) and predicted glycosyltransferases (19). The basal ECM of rosettes is reminiscent of the basal lamina, a basally secreted layer of ECM that underpins animal epithelia and regulates tissue morphogenesis by constraining cell

358 proliferation (29) including in *Drosophila* wing and egg chamber development (54,
359 61, 62), branching growth during lung and salivary gland development (63, 64),
360 notochord expansion (65), lumen elongation (66), and in tumor growth in
361 mammary epithelia (45). The ECM also sculpts morphogenesis in *Volvox*, in which
362 defects in ECM composition disrupt morphogenesis (67, 68), and in bacterial
363 biofilms, in which the ECM can constrain cells and thereby drive 3D morphogenesis
364 (26, 69). Remarkably, some bacteria form multicellular rosettes in a process that is
365 mediated by basal ECM secretion (70, 71).

366 Altogether, the principles that we can glean from the simplicity of
367 choanoflagellate morphogenesis holds the promise of revealing general principles
368 by which biological and physical mechanisms shape morphogenesis more broadly.

Methods

Choanoflagellate strains and culture

Two strains of *S. rosetta* were used for the experiments in this study: one grown solely in the presence of the non-rosette inducing bacterium *Echinicola pacifica* (72), a strain called SrEpac (73) and the other grown solely in the presence of the rosette inducing bacterium *Algoriphagus machipongonensis* (74), a strain called PX1 (23, 75).

SrEpac was grown in 5% Sea Water Complete (SWC) media at 22°C. Sea Water Complete media consisted of 250 mg/L peptone, 150 mg/L yeast extract, 150µL/L glycerol in artificial sea water and was diluted to 5% by volume in artificial sea water to make 5% Sea Water Complete media. Artificial sea water (ASW) consisted of 32.9 g Tropic Marin sea salts (Wartenberg, Germany) dissolved in 1L distilled water for a final salinity of 32-27 parts per thousand. SrEpac was passaged either 1:10 into 9mL fresh 5% SWC once a day or 1:20 every other day into 9mL fresh 5% SWC to stimulate rapid proliferation and maintain log-phase growth. Cells were grown in 25cm^2 cell culture flask (Corning).

PX1 was grown in 25% Cereal Grass media (CGM3) at 22°C. Cereal Grass media consisted of Cereal Grass (Basic Science Supplies) added to ASW at 5g/L, steeped for 3.5 hours and then filtered. This media was then diluted to 5% by volume in ASW in order to make 25% CGM3. PX1 was passaged 1:5 into 9mL of fresh 25% CGM3 every two to three days to stimulate rapid proliferation and maintain log-phase growth. Cells were grown in 25cm^2 cell culture flask (Corning).

392 ***Rosette induction***

393 Rosette development from single cells was stimulated by the addition of
394 outer membrane vesicles (OMVs) isolated from *Algoriphagus* bacteria (23) to
395 SrEpac cultures. To isolate OMVs, *Algoriphagus* was first grown in 200mL of SWC at
396 30°C for 48 hrs. on a shaker. Bacterial cells were then pelleted, and the cell free
397 supernatant was sterile filtered, then spun at 36,000 x g for three hours at 4°C (Type
398 45 Ti rotor, Beckman Coulter) to pellet OMVs. Finally, OMVs were resuspended in
399 1.5 mL ASW. To induce rosette development, OMVs were added to SrEpac at a
400 concentration of 1:2000 by volume. This concentration led to >90% of cells in
401 rosettes by 48 hrs. post-induction.

402

403 ***Electron microscopy***

404 *Algoriphagus* OMV induced SrEPac cultures (48 hours post-induction) were
405 concentrated by centrifugation (1200xg for 5 min). Colonies were resuspended in
406 5% BSA in ASW, high pressure frozen using a Leica EM PACT2, and fixed by freeze
407 substitution in 0.01% OsO_4 + 0.2% uranyl acetate in acetone (76). Samples were
408 resin embedded in Epon Araldite (Embed-812) (77), cut into 80 nm sections, and
409 then imaged using an FEI Tecnai 12 transmission electron microscope.

410

411 ***Rosette cell number quantification***

412 Rosettes from rapidly growing PX1 cultures (*S. rosetta* co-cultured with
413 *Algoriphagus*) were concentrated to 5x by centrifugation (1500xg for 10 min) and
414 resuspended by vigorous pipetting in fresh 25% CGM3 media. Rosettes were then

415 gently adhered to a poly-D-lysine coated coverslip (FluoroDish, World Precision
416 Instruments, Inc), which had been washed three times using 25% CGM3. Rosettes
417 were observed using a Leica DMIL microscope with a 20x objective (Leica, N Plan,
418 0.35 NA), and cells were manually counted. In general, rosettes were not
419 overlapping, and cells were deemed to belong to a rosette when oriented radially
420 outward about a central focus.
421
422 ***Quantitative morphology analysis pipeline***
423 For morphological analysis of rosettes, SrEpac cultures were first induced to
424 form rosettes as described above. After 24 hours, developing rosettes were pelleted
425 by centrifugation (1500xg for 10 min) and resuspended in fresh ASW by vigorous
426 pipetting in order to minimize bacteria and to break apart any chains that might be
427 mistaken for rosettes. Rosettes were then deposited onto a poly-D-lysine coated
428 coverslip (FluoroDish, World Precision Instruments, Inc), which had been washed
429 three times using ASW. Rosettes were stained by overloading with LysoTracker Red
430 DND-99 (ThermoFisher Scientific) at 1:200 dilution, which reliably stains the entire
431 cell body. Next, z-stack images of stained rosettes were acquired on a Zeiss 880 laser
432 scanning confocal microscope using a 40x water immersion objective (Zeiss, C-
433 Apochromat, 1.2 NA) and illumination with a 561 nm laser (Zeiss). Importantly,
434 pure water, and not water immersion oil, was used to minimize coverslip deflection
435 during imaging.
436 After image acquisition, z-stacks were registered using the Stackreg plugin in
437 FIJI (78, 79). Aligned z-stacks were deconvolved using the Parallel Iterative

Deconvolution v1.12 plugin in FIJI (78, 79). For deconvolution, the Wiener Filter Preconditioned Landweber method (WPL) with stock settings and a theoretical pointspread function for the imaging system generated using the Diffraction PSF 3D plugin in FIJI (78, 79) were used. Aligned, deconvolved z-stacks were then segmented using Imaris v3.8 (Bitplane, Belfast). First, the images were median filtered with a 3x3x1 kernel and smoothed using a Gaussian filter with a sigma of 0.24 microns. Intensity thresholds for local intensity segmentation and thresholds for size and shape filters to exclude extraneous objects such as bacteria within the analysis region were then chosen based on segmentation of a few rosettes from each sample and then kept the same for all rosettes in the sample. Individual cells in rosettes were segmented using the Split Touching Objects option. Segmentation of each rosette was manually inspected, and any improperly segmented cells were manually split and fused as necessary. Statistics of segmented rosettes, including number of cells, cell positions, orientations, sizes, and shapes were exported to MATLAB release 2016a (Mathworks, Natick) for additional morphological analysis.

Rosette volume was measured by determining the convex hull of cell positions. Maximum rosette width was measured by the maximum distance between cells in rosettes. To further evaluate rosette morphology, principle axes of rosettes were determined by principle components analysis of cell positions. Flatness (F) and Sphericity (S) of rosettes were computed from these principle components where $F = 1 - C/B$, and $S = \sqrt[3]{BC/A^2}$ where A, B, and C are the principle axes in descending order of magnitude. The packing of cells was then quantified by the average number of neighboring cells over all cells in rosettes as

461 determined by a Voronoi tessellation (80) of cell positions. Finally, rosettes were
462 then binned by cell number for the final analysis of morphological progression.
463
464 ***Cell lineage analysis***
465 Rapidly growing SrEpac cultures were induced to form rosettes, and 9 hours
466 post induction, induced cells were concentrated to 5x by centrifugation and
467 resuspension in 5% SWC (1200xg for 5 min, initial volume 15mL resuspended in
468 3mL) and then deposited in a 200 μL droplet on a poly-D-lysine coated coverslip
469 (FluoroDish, World Precision Instruments, Inc). Cells were imaged in phase contrast
470 or DIC on either a Zeiss Axio Observer Z1 with a 20x (Zeiss, Plan-Apochromat, 0.8
471 NA) objective or a Leica DMI6000B with a 20x (Leica, Plan-Apochromat, 0.7 NA)
472 objective at 1 frame/minute for 16 hours. Cell positions were tracked using the
473 Manual Tracking plugin in FIJI (78, 79), and division events were tracked and
474 recorded manually. For analysis of chain cell lineages, the cells were not induced to
475 form rosettes, but otherwise all previous steps were followed.
476
477 ***ECM measurements***
478 Rosettes were prepared as in the "Quantitative morphology analysis
479 pipeline" section (QMAP). Additionally, to label the ECM, fluorescein labeled Jacalin
480 (Vector Labs, FL-1151) at a 1:400 dilution was added to the concentrated rosettes.
481 Imaging also followed the QMAP with additional sequential illumination with a 488
482 nm laser to excite the fluorescein. Z-stack images were processed and analyzed

following QMAP with the exception of post-processing in MATLAB, as cell and ECM volumes were exported directly from Imaris.

Laser ablation

For laser ablation, an upright Olympus BX51WI microscope (Olympus Corporation) equipped with Swept Field Confocal Technology (Bruker) and a Ti:Sapphire 2-photon Chameleon Ultra II laser (Coherent) were used. The 2-photon laser was set to 770 nm and ablation was performed using three 20 ms pulses. A 60x water dipping objective (Olympus, LUMPlanFL N, 1.0 NA) was used for imaging. Images were captured using an EM-CCD camera (Photometrics). The following emission filter was used: Quad FF-01-446/523/600/677-25 (Semrock). PrairieView Software (v. 5.3 U3, Bruker) was used to acquire images.

Rosettes were gently adhered to a coverslip using poly-D-lysine and stained with lysotracker (as described above). Individual cells in rosettes were ablated, and the subsequent recoil, which is proportional to the elastic stress (7, 39, 43), was recorded at a frame rate of 1/0.48 s. Images were registered using the StackReg plugin in FIJI (78, 79) to correct for small movements of the rosette colony due to flagellar motion during acquisition of images. Recoil velocities were measured in the frames following ablation by particle image velocimetry (PIV) using PIVlab software in MATLAB (81). Settings for PIV included four direct Fourier transform correlation passes with window sizes of 64, 32, 16 and 8 pixels and corresponding step sizes of 32, 16, 8, and 4 pixels. To reject noise and erroneous velocities, filters of 7 standard deviations about the mean and local median filters with a threshold of 5 and epsilon

of 0.1 were applied. Finally, any remaining velocity measurements not corresponding to displacements of cells in rosettes were manually rejected. Recoil velocities were measured in the subsequent 3 frames following ablation by radial scans about the circumference of the rosette, and the maximum measured velocity was selected.

Strontium treatment

For strontium treatment of rosettes, SrEpac cultures were centrifuged at 1500g for 10 to pellet all cells and resuspended in 5% SWC media containing added $SrCl_2$ to a final concentration of either 0, 2.5, or 5 mM. These cells were then induced to form rosettes as described above. Morphological analysis and laser ablation were also conducted as described above.

For cell growth assays (Fig. S4), SrEpac cultures were prepared as described in the preceding paragraph but were not induced to form rosettes. Cells were then plated into 12-well plates (Falcon) at an initial density of 20000 cells/mL. To determine cell density, cells were counted using a hemocytometer (Hausser Scientific) viewed in phase contrast on a Leica DMIL microscope with a 20x (Leica, N Plan, 0.35 NA) objective. Cells were counted at 4, 24, and 28 hours. Growth rates were then determined by exponential fits to the log-phase of growth obtained using the Curve Fitting application in MATLAB.

Simulations

Cells and ECM were modelled as spherical particles (Fig. 6) with interactions that allowed us to tune the various morphological and material properties we wished to investigate. The particle representation allowed us to capture both the relevant geometric aspects of colony formation including polarized cell divisions and ECM secretion as well as the discrete and stochastic nature of these processes.

Cells

Each cell was composed of three linked particles with diameters d_1, d_2, and d_3 representing the basal pole, cell body, and collar and in ascending order of magnitude, to capture cell geometry. Cell particles interacted sterically with one another via the hard-sphere Weeks-Chandler-Andersen (WCA) potential (82):

$$V_{WCA}(R) = 4\varepsilon_{WCA}\left[\left(\frac{d_i}{R}\right)^{12} - \left(\frac{d_i}{R}\right)^{6}\right] + \Delta V(R) \text{ for } R < R_{cut}, \text{ and}$$

$$V_{WCA}(R) = 0 \text{ for } R > R_{cut}$$

where R is the interparticle distance; d_i with $i = 1, 2, 3$ is the cell particle diameter; ε_{WCA} sets the force of repulsion upon overlap; $\Delta V(R) = V_{LJ}(R_{cut})$ where V_{LJ} is the Lennard-Jones potential (82):

$$V_{LJ}(R) = 4\varepsilon\left[\left(\frac{d_i}{R}\right)^{12} - \left(\frac{d_i}{R}\right)^{6}\right]$$

with $\varepsilon = \varepsilon_{WCA}$; and $R_{cut} = 2^{\frac{1}{6}}d_i$ is the cutoff distance for the potential set to the diameter of the cell particle. For a given cell, cohesion of particles was maintained using a finitely extensible nonlinear elastic (FENE) potential:

$$V_{FENE}(R) = \frac{1}{2}k_{FENE}R_0^2\left(1 - \left(\frac{R-\Delta}{R_0}\right)^2\right) + V_{WCAS}(R)$$

where k_{FENE} sets the strength of the potential; $R_0 = d_1$ (set to maintain cohesion); R is the interparticle distance; $\Delta = \frac{d_i + d_j}{2} - d_1$ where d_k is the diameter of the k^{th} particle; and

$$V_{WCAS}(R) = 4\varepsilon_{WCA}\left[\left(\frac{d_i}{R-\Delta}\right)^{12} - \left(\frac{d_i}{R-\Delta}\right)^{6}\right] \text{ for } R - \Delta < 2^{\frac{1}{6}}\Delta, \text{ and}$$

$$V_{WCAS}(R) = 0 \text{ for } R - \Delta \geq 2^{\frac{1}{6}}\Delta.$$

Additionally, a harmonic potential acting between the basal and apical cell particle was used to keep cells straight and elongated:

$$V_h(R) = \frac{1}{2}k(R - R_E)^2$$

where the spring constant $k = k_h$ sets the strength of the potential, and rest length $R_E = 2(d_1/2 + d_2 + d_3/2)$ was chosen to be large enough to ensure cell elongation. For simplicity, the mass of all cell particles was the same, and the friction coefficient was otherwise determined by viscosity, η and the particle diameter, d: $\gamma = 6\pi\eta d$.

ECM

ECM was composed of small particles with diameter $d_{ECM} \ll d_1$. To maintain ECM cohesion (while preventing divergence in energy) and volume, allow for ECM deformations and shape transformation, and for computational tractability, ECM-ECM particle interactions were also modeled by a modified Lennard-Jones potential (83), which reduces interparticle repulsion and better describes a condensed state, such as ECM:

$$V_{MLJ}(R) = 4\varepsilon\left[\left(\frac{d_{ECM}}{R}\right)^{4} - \left(\frac{d_{ECM}}{R}\right)^{2}\right] \text{ for } R < R_{cut}, \text{ and}$$

$$V_{MLJ}(R) = 0 \text{ for } R > R_{cut}$$

where R is the interparticle distance, $\varepsilon = \varepsilon_{ECM}$ sets the strength of ECM adhesion, and $R_{cut} = 2^{\frac{1}{6}} d_{ECM}$ is the cutoff distance for the potential.

Cell-ECM interactions

To capture adhesive interactions while preventing particle overlap and for computational tractability, cell-ECM adhesion was modeled with a modified Lennard-Jones potential between basal cell particles and ECM particles:

$$V_{SLJ}(R) = 4\varepsilon_{ECM}\left[\left(\frac{d_{ECM}}{R-\Delta}\right)^{12} - \left(\frac{d_{ECM}}{R-\Delta}\right)^{6}\right] \text{ for } R < R_{cut} + \Delta, \text{ and}$$

$$V_{SLJ}(R) = 0 \text{ for } R \geq R_{cut} + \Delta$$

where $R_{cut} = 2^{\frac{1}{6}} d_{ECM}$, and $\Delta = \frac{d_{ECM}+d_1}{2} - d_1$.

Cell division

Cells were allowed to divide stochastically, with probability $p_{Div}(t) = \frac{1}{1-e^{-\mu(t-\tau_{Div})}}$ where τ_{Div} is the cell cycle time, and $\mu = \frac{\tau_{Div}}{10}$ sets the variability in division timing. The division plane orientation around the apico-basal axis was set by the previous division. During division, cell particles are replicated and shifted slightly (starting with a separation $0.25 d_i$ for particle i) in the direction perpendicular to the division plane by an offset D_{Div}. Dividing cell particles then push one another apart under the influence of a harmonic potential with increasing rest length: $V_h(R) = \frac{1}{2} k (R - R_P)^2$ where the spring constant $k = k_{Div}$ sets the strength of the potential, and hence, how much force the cells can exert during growth and division; and rest length R_P increases with each timestep in the simulation by an amount $\delta R = \frac{(d_i + 2^{\frac{1}{6}} - 1)}{g_{Div}}$ where g_{DIV} is the number of timesteps over

which division occurs for particle i. Cell division is complete once $R_P \geq d_i$ for all particles. With this implementation of cell division, we approximated both cell growth (while particles are still overlapping) and division.

ECM secretion

ECM particles were secreted stochastically from non-dividing cells at a constant rate with a probability $1 - p_{Div}(t)$ from the basal pole of non-dividing cells. Secretion always occurred in the direction of the apico-basal axis of cells. Similarly to division, ECM particles were extended from the basal pole according to a harmonic potential with $k = k_{ECM}$ setting the force with which ECM particles were secreted; the rest length R_P increased with every time step by $\delta R = \frac{(d_{ECM}+2^{\frac{1}{6}}-1)}{g_{SEC}}$ where g_{SEC} is the number of timesteps over which secretion occurs. Secretion is complete once $R_P = \frac{d_1+d_{ECM}}{2}$.

Running simulations

Simulations were carried out using Fortran and followed Brownian dynamics (84):

$$\dot{X} = \frac{\sqrt{\gamma k_B T} D(t) - \nabla U(X)}{\gamma},$$

where X and $\dot{X}$ are position and velocity; $U(X)$ is the sum of all interaction potentials acting on a given element of the system (particle), so $-\nabla U(X)$ with ∇ as the gradient operator, is the force resulting from the total interaction potential on a given element of the system (particle); γ is the friction coefficient, $k_B$is Boltzmann's constant, T is temperature, and $D(t)$ is a delta correlated, stationary Gaussian process with 0 mean. For simplicity, the mass of all particles was the same, and the

612 friction coefficient was otherwise determined by viscosity, η and the particle
613 diameter, d: $\gamma = 6\pi\eta d$. A Verlet integration algorithm was used to update the
614 positions of the spheres at each timestep in the simulation (85).
615 Code for running simulations is available on GitHub:
616 https://github.com/truizherrero/choanoflagellate_colonies.

617 **Simulation analysis**

618 In the model, three main parameters corresponding to physical aspects of
619 choanoflagellate cells and rosettes describe the system: 1) cell aspect ratio, defined
620 to be the length to width ratio of the three particle system: $\frac{d_1+d_2+d_3}{d_3}$; 2) scaled ECM
621 stiffness relative to the force exerted during cell growth and division: $\frac{\varepsilon_{ECM}}{k_{Div}d_1^2}$; and 3)
622 The ECM volume relative to cell volume secreted by a cell between divisions:
623 $\frac{nd_{ECM}^3}{2(d_1^3+d_2^3+d_3^3)}$ where $n = \frac{\tau_{Div}}{\tau_{Sec}}$ with $\tau_{Sec} = \frac{R_P}{\delta R}$ is the average number of ECM particles
624 secreted between divisions.

625 Natural units for the system are the length d_1, time τ_{Div}, and energy k_BT. For
626 all simulations, the following values in system units were held fixed: $k_{FENE} =$
627 $500\ \frac{k_BT}{d_1^2}$, $\eta = 50\ \frac{k_BT\tau_{Div}}{d_1^3}$, $k_h = 200\ \frac{k_BT}{d_1^2}$, $g_{Div} = 5000\ \frac{d_1^3}{\tau_{Div}}$, and $g_{Sec} = 5000\ \frac{d_1^3}{\tau_{Div}}$. All
628 other parameters not already fixed in the previous paragraphs were varied to
629 explore the morphospace (Fig. 6B), with axes corresponding to the three main
630 parameters detailed in the previous section. The timestep for simulations was
631 $0.001\tau_{Div}$. Simulation snapshots for Fig. 6 were rendered for the visual inspection of
632 morphologies using Python. Rosettes were defined as structures with cells
633 completely surrounding a central region of ECM; disks were defined as structures

634 that maintained a closed ring of cells pointing radially outward along the colony
635 circumference with an open central region of ECM; cups and cones were defined as
636 structures with cells clustered together, oriented in roughly the same direction,
637 opposed to an open ECM emanating away from the basal pole of all cells; and trees
638 were defined as structures with cells oriented in a similar fashion to those in cones
639 but with the ECM displaying a dichotomous branching structure. Quantitative
640 analyses of simulation results (Fig. S5) were carried out in MATLAB.

Acknowledgements:

We thank Kent McDonald and Reena Zalpuri of the Electron Microscopy Laboratory at UC Berkeley for assistance with TEM sample preparation and imaging. We would also like to thank Mary West of the CIRM/QB3 Shared Stem Cell Facility at UC Berkeley. Additionally, we thank George Oster and Danny Wells for helpful discussions concerning conceptual development of this project. Finally, we thank the members of the King Lab for critical feedback and stimulating discussions. This work was performed in part in the SSCF, which provided the Olympus BX51WI microscope with Swept Field Confocal technology. This material is based upon work supported by the National Science Foundation Graduate Research Fellowship under Grant No. DGE 1106400 (to B.T.L.), the Simons Foundation (T.R.H.) the Howard Hughes Medical Institute (N.K.), and the National Institutes of Health (NIH) under award numbers F31GM119329 (to S.L.), R01GM122375 (to S.K.), and R21EB016359 (to S.K.).

655 1. Harvey W (1651) *Exercitationes de generatione animalium. Quibus accedunt*
656 *quaedam de partu: de membranis ac humoribus uteri: & de conceptione* (Typis
657 Du-Gardianis, London) doi:https://doi.org/10.5962/bhl.title.44364.
658 2. Gilbert SF (2000) *Developmental biology* (Sinauer Associates, Sunderland).
659 3. Golling G, et al. (2002) Insertional mutagenesis in zebrafish rapidly identifies
660 genes essential for early vertebrate development. *Nat Genet* 31(2):135–140.
661 4. Xue Z, et al. (2013) Genetic programs in human and mouse early embryos
662 revealed by single-cell RNA sequencing. *Nature* 500(7464):593–597.
663 5. Chen B-C, et al. (2014) Lattice light-sheet microscopy: imaging molecules to
664 embryos at high spatiotemporal resolution. *Science* 346(6208):1257998.
665 6. Keller PJ, Schmidt AD, Wittbrodt J, Stelzer EHK (2008) Reconstruction of
666 zebrafish early embryonic development by scanned light sheet microscopy.
667 *Science* 322(5904):1065–9.
668 7. Behrndt M, et al. (2012) Forces Driving Epithelial Spreading in Zebrafish
669 Gastrulation. *Science (80-)* 338(6104):257–260.
670 8. Mayer M, Depken M, Bois JS, Jülicher F, Grill SW (2010) Anisotropies in
671 cortical tension reveal the physical basis of polarizing cortical flows. *Nature*
672 467(7315):617–621.
673 9. Bailles A, et al. (2018) Transcriptional initiation and mechanically driven self-
674 propagation of a tissue contractile wave during axis elongation.
675 *bioRxiv*:430512.
676 10. Carr M, Leadbeater BSC, Hassan R, Nelson M, Baldauf SL (2008) Molecular
677 phylogeny of choanoflagellates, the sister group to Metazoa. *Proc Natl Acad Sci*

105(43). doi:10.1073/pnas.0801667105.

11. King N, et al. (2008) The genome of the choanoflagellate Monosiga brevicollis and the origin of metazoans. *Nature* 451(7180):783–788.

12. Ruiz-Trillo I, Roger AJ, Burger G, Gray MW, Lang BF (2008) A Phylogenomic Investigation into the Origin of Metazoa. *Mol Biol Evol* 25(4):664–672.

13. Leadbeater BSC (2015) *The Choanoflagellates* (Cambridge University Press, Cambridge) doi:10.1017/CBO9781139051125.

14. Brunet T, King N (2017) The Origin of Animal Multicellularity and Cell Differentiation. *Dev Cell* 43(2):124–140.

15. Leadbeater BSC (1983) Life-history and ultrastructure of a new marine species of Proterospongia (Choanoflagellida). *J Mar Biol Assoc United Kingdom* 63(01):135.

16. Dayel MJ, et al. (2011) Cell differentiation and morphogenesis in the colony-forming choanoflagellate Salpingoeca rosetta. *Dev Biol* 357(1):73–82.

17. Fairclough SR, Dayel MJ, King N (2010) Multicellular development in a choanoflagellate. *Curr Biol* 20(20):R875–R876.

18. Levin TC, Greaney AJ, Wetzel L, King N (2014) The rosetteless gene controls development in the choanoflagellate S. rosetta. *Elife* 3. doi:10.7554/eLife.04070.

19. Wetzel LA, et al. (2018) Predicted glycosyltransferases promote development and prevent spurious cell clumping in the choanoflagellate S. rosetta. *Elife* 7. doi:10.7554/eLife.41482.

20. Sulston JE, Schierenberg E, White JG, Thomson JN (1983) The embryonic cell

lineage of the nematode Caenorhabditis elegans. *Dev Biol* 100(1):64–119.

21. Leys SP, Ereskovsky A V (2006) Embryogenesis and larval differentiation in sponges. *Can J Zool* 84(2):262–287.

22. Lewis WH, Wright ES (1935) *On the early development of the mouse egg* (Carnegie Institution of Washington, Washington).

23. Alegado RA, et al. (2012) A bacterial sulfonolipid triggers multicellular development in the closest living relatives of animals. *Elife* 1:e00013.

24. Woznica A, et al. (2016) Bacterial lipids activate, synergize, and inhibit a developmental switch in choanoflagellates. *Proc Natl Acad Sci U S A* 113(28):7894–9.

25. Hannezo E, Prost J, Joanny J-F Theory of epithelial sheet morphology in three dimensions. *Proc Natl Acad Sci U S A*. doi:10.1073/pnas.1312076111.

26. Yan J, Sharo AG, Stone HA, Wingreen NS, Bassler BL (2016) Vibrio cholerae biofilm growth program and architecture revealed by single-cell live imaging. *Proc Natl Acad Sci U S A* 113(36):E5337-43.

27. Savin T, et al. (2011) On the growth and form of the gut. *Nature* 476(7358):57–62.

28. Forgács G, Newman SA (2005) *Biological physics of the developing embryo* (Cambridge University Press, Cambridge).

29. Ingber DE (2006) Mechanical control of tissue morphogenesis during embryological development. *Int J Dev Biol* 50(2–3):255–266.

30. Deppe U, et al. (1978) Cell lineages of the embryo of the nematode Caenorhabditis elegans. *Proc Natl Acad Sci* 75(1):376–380.

724 31. Newport J, Kirschner M (1982) A major developmental transition in early
725 Xenopus embryos: I. characterization and timing of cellular changes at the
726 midblastula stage. *Cell* 30(3):675–86.
727 32. Kane DA, Kimmel CB (1993) The zebrafish midblastula transition.
728 *Development* 119(2):447–56.
729 33. Edgar BA, O'Farrell PH (1989) Genetic control of cell division patterns in the
730 Drosophila embryo. *Cell* 57(1):177–87.
731 34. Bišová K, Zachleder V (2014) Cell-cycle regulation in green algae dividing by
732 multiple fission. *J Exp Bot* 65(10):2585–2602.
733 35. Umen JG, Olson BJSC (2012) Genomics of Volvocine Algae. *Adv Bot Res*
734 64:185–243.
735 36. Matt G, Umen J (2016) Volvox: A simple algal model for embryogenesis,
736 morphogenesis and cellular differentiation. *Dev Biol* 419(1):99–113.
737 37. Laundon D, Larson B, McDonald K, King N, Burkhardt P (2018) The
738 architecture of cell differentiation in choanoflagellates and sponge
739 choanocytes. *bioRxiv*:452185.
740 38. Roque-Barreira MC, Praz F, Halbwachs-Mecarelli L, Greene LJ, Campos-Neto A
741 (1986) IgA-affinity purification and characterization of the lectin jacalin. *Rev*
742 *Bras Pesqui Med Biol* 19(2):149–57.
743 39. Ma X, Lynch HE, Scully PC, Hutson MS (2009) Probing embryonic tissue
744 mechanics with laser hole drilling. *Phys Biol* 6(3):036004.
745 40. Hutson MS, et al. (2009) Combining Laser Microsurgery and Finite Element
746 Modeling to Assess Cell-Level Epithelial Mechanics. *Biophys J* 97(12):3075–

3085.

41. Rauzi M, Lenne P-F (2011) Cortical Forces in Cell Shape Changes and Tissue Morphogenesis. *Curr Top Dev Biol* 95:93–144.

42. Bonnet I, et al. (2012) Mechanical state, material properties and continuous description of an epithelial tissue. *J R Soc Interface* 9(75):2614–23.

43. Hutson MS, et al. (2003) Forces for morphogenesis investigated with laser microsurgery and quantitative modeling. *Science* 300(5616):145–9.

44. Kuo CK, Ma PX (2001) Ionically crosslinked alginate hydrogels as scaffolds for tissue engineering: Part 1. Structure, gelation rate and mechanical properties. *Biomaterials* 22(6):511–521.

45. Chaudhuri O, et al. (2014) Extracellular matrix stiffness and composition jointly regulate the induction of malignant phenotypes in mammary epithelium. *Nat Mater* 13(10):970–978.

46. Ryan EA, Mockros LF, Weisel JW, Lorand L (1999) Structural Origins of Fibrin Clot Rheology. *Biophys J* 77(5):2813–2826.

47. Wilkie IC, et al. (2006) Mechanical adaptability of a sponge extracellular matrix: evidence for cellular control of mesohyl stiffness in Chondrosia reniformis Nardo. *J Exp Biol* 209(22):4436–4443.

48. Mo J, et al. (2016) Interfibrillar stiffening of echinoderm mutable collagenous tissue demonstrated at the nanoscale. *Proc Natl Acad Sci U S A* 113(42):E6362–E6371.

49. Purcell EM (1977) Life at low Reynolds number. *Am J Phys* 45(1):3–11.

50. Higdon JJL (1979) The generation of feeding currents by flagellar motions. *J*

Fluid Mech 94(02):305.

51. Raup DM (1967) Geometric Analysis of Shell Coiling: Coiling in Ammonoids. *JPaleo* 41(1):43–65.

52. Calkins GN (1914) *Biology* (Henry Holt and Company, New York) doi:https://doi.org/10.5962/bhl.title.24281.

53. Saville-Kent W (1881) *A manual of the Infusoria : including a description of all known flagellate, ciliate, and tentaculiferous protozoa, British and foreign, and an account of the organization and the affinities of the sponges* (David Bogue, London) doi:https://doi.org/10.5962/bhl.title.1243.

54. Hufnagel L, Teleman AA, Rouault H, Cohen SM, Shraiman BI (2007) On the mechanism of wing size determination in fly development. *Proc Natl Acad Sci* 104(10):3835–3840.

55. Shyer AE, et al. (2013) Villification: How the gut gets its villi. *Science (80-)* 342(6155):212–218.

56. Jacobeen S, et al. (2018) Cellular packing, mechanical stress and the evolution of multicellularity. *Nat Phys* 14(3):286–290.

57. Petridou NI, Spiró Z, Heisenberg C-P (2017) Multiscale force sensing in development. *Nat Cell Biol* 19(6):581–588.

58. Shraiman BI (2005) Mechanical feedback as a possible regulator of tissue growth. *Proc Natl Acad Sci U S A* 102(9):3318–23.

59. Guillot C, Lecuit T (2013) Mechanics of epithelial tissue homeostasis and morphogenesis. *Science* 340(6137):1185–9.

60. Moreno E, Valon L, Levillayer F, Levayer R (2018) Competition for Space

Induces Cell Elimination through Compaction-Driven ERK Downregulation. *Curr Biol* 29(1):23-34.e8.

61. Pastor-Pareja JC, Xu T (2011) Shaping cells and organs in Drosophila by opposing roles of fat body-secreted Collagen IV and perlecan. *Dev Cell* 21(2):245–56.

62. Crest J, Diz-Muñoz A, Chen D-Y, Fletcher DA, Bilder D (2017) Organ sculpting by patterned extracellular matrix stiffness. *Elife* 6. doi:10.7554/eLife.24958.

63. Moore KA, et al. (2005) Control of basement membrane remodeling and epithelial branching morphogenesis in embryonic lung by Rho and cytoskeletal tension. *Dev Dyn* 232(2):268–281.

64. Harunaga JS, Doyle AD, Yamada KM (2014) Local and global dynamics of the basement membrane during branching morphogenesis require protease activity and actomyosin contractility. *Dev Biol* 394(2):197–205.

65. Adams DS, Keller R, Koehl MA (1990) The mechanics of notochord elongation, straightening and stiffening in the embryo of Xenopus laevis. *Development* 110(1).

66. Li Q, et al. (2016) Extracellular matrix scaffolding guides lumen elongation by inducing anisotropic intercellular mechanical tension. *Nat Cell Biol* 18(3):311–318.

67. Hallmann A, Kirk DL (2000) The developmentally regulated ECM glycoprotein ISG plays an essential role in organizing the ECM and orienting the cells of Volvox. *J Cell Sci* 113(24).

68. Ueki N, Nishii I Controlled Enlargement of the Glycoprotein Vesicle

816 Surrounding a Volvox Embryo Requires the InvB Nucleotide-Sugar
817 Transporter and Is Required for Normal Morphogenesis W. *Plant Cell*.
818 doi:10.1105/tpc.109.066159.
819 69. Drescher K, et al. (2016) Architectural transitions in Vibrio cholerae biofilms
820 at single-cell resolution. *Proc Natl Acad Sci U S A* 113(14):E2066-72.
821 70. Moore RL, Marshall KC (1981) Attachment and rosette formation by
822 hyphomicrobia. *Appl Environ Microbiol* 42(5):751–7.
823 71. Frank O, et al. (2015) Plasmid curing and the loss of grip – The 65-kb replicon
824 of Phaeobacter inhibens DSM 17395 is required for biofilm formation,
825 motility and the colonization of marine algae. *Syst Appl Microbiol* 38(2):120–
826 127.
827 72. Nedashkovskaya OI, et al. (2006) Echinicola pacifica gen. nov., sp. nov., a novel
828 flexibacterium isolated from the sea urchin Strongylocentrotus intermedius.
829 *Int J Syst Evol Microbiol* 56(5):953–958.
830 73. Levin TC, King N (2013) Evidence for Sex and Recombination in the
831 Choanoflagellate Salpingoeca rosetta. *Curr Biol* 23(21):2176–2180.
832 74. Alegado RA, et al. (2013) Algoriphagus machipongonensis sp. nov., co-isolated
833 with a colonial choanoflagellate. *Int J Syst Evol Microbiol* 63(Pt 1):163–8.
834 75. Fairclough SR, et al. (2013) Premetazoan genome evolution and the regulation
835 of cell differentiation in the choanoflagellate Salpingoeca rosetta. *Genome Biol*
836 14(2):R15.
837 76. McDonald KL, Webb RI (2011) Freeze substitution in 3 hours or less. *J Microsc*
838 243(3):227–233.

77. McDonald KL (2014) Rapid Embedding Methods into Epoxy and LR White Resins for Morphological and Immunological Analysis of Cryofixed Biological Specimens. *Microsc Microanal* 20(01):152–163.

78. Schindelin J, et al. (2012) Fiji: an open-source platform for biological-image analysis. *Nat Methods* 9(7):676–682.

79. Schneider CA, Rasband WS, Eliceiri KW (2012) NIH Image to ImageJ: 25 years of image analysis. *Nat Methods* 9(7):671–675.

80. Voronoi G (1908) Nouvelles applications des paramètres continus à la théorie des formes quadratiques. Premier mémoire. Sur quelques propriétés des formes quadratiques positives parfaites. *J für die reine und Angew Math* 133:97–178.

81. Ryerson WG, Schwenk K (2012) A simple, inexpensive system for digital particle image velocimetry (DPIV) in biomechanics. *J Exp Zool Part A Ecol Genet Physiol* 317(2):127–140.

82. Weeks JD, Chandler D, Andersen HC (1971) Role of Repulsive Forces in Determining the Equilibrium Structure of Simple Liquids. *J Chem Phys* 54(12):5237–5247.

83. Jones JE (1924) On the Determination of Molecular Fields. I. From the Variation of the Viscosity of a Gas with Temperature. *Proc R Soc A Math Phys Eng Sci* 106(738):441–462.

84. Doyle PS, Underhill PT (2005) Brownian Dynamics Simulations of Polymers and Soft Matter. *Handbook of Materials Modeling* (Springer Netherlands, Dordrecht), pp 2619–2630.

862 85. Verlet L (1967) Computer "Experiments" on Classical Fluids. I.
863 Thermodynamical Properties of Lennard-Jones Molecules. *Phys Rev*
864 159(1):98–103.
865 86. Haeckel E (1904) *Kunstformen der Natur* (Verlag des Bibliographischen
866 Instituts, Leipzig, Wien).
867 87. Richter DJ, Fozouni P, Eisen MB, King N (2018) Gene family innovation,
868 conservation and loss on the animal stem lineage. *Elife* 7.
869 doi:10.7554/eLife.34226.
870 88. Ertl M (1981) Zur taxonomie der Gattung ProterospongiaKent. *Arch für*
871 *Protistenkd* 124(3):259–266.
872 89. Wadell H Volume, Shape, and Roundness of Quartz Particles. *Source J Geol*
873 43(3):250–280.
874

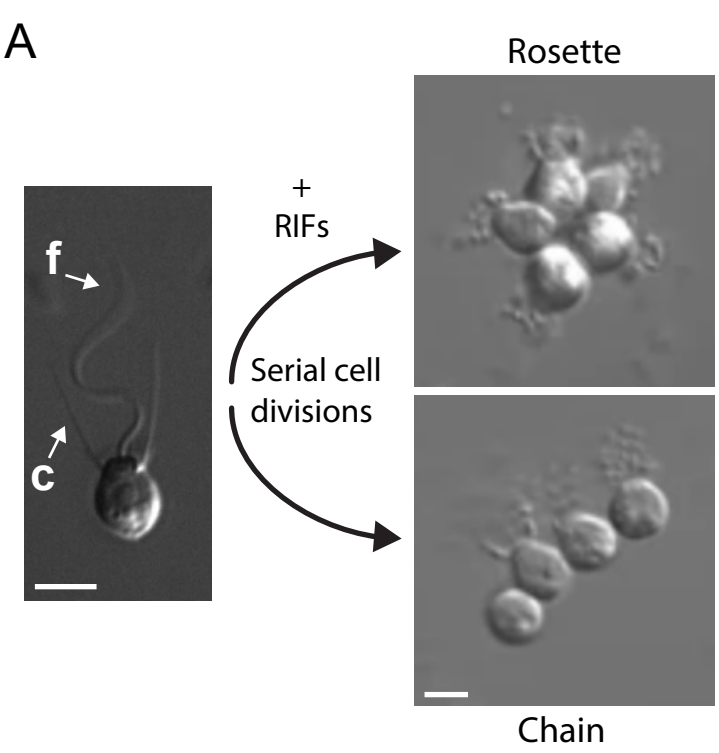

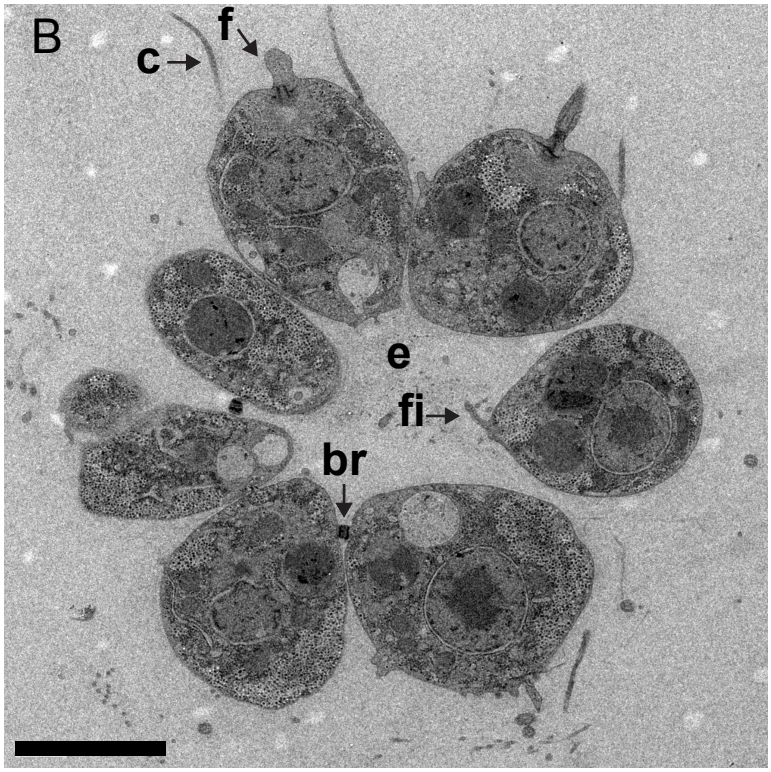

875 **Figure 1. The choanoflagellate *Salpingoeca rosetta* develops from a single cell**
876 **into multicellular colonies through serial rounds of cell divisions** (17). (**A**) All
877 choanoflagellate cells bear a diagnostic "collar complex" composed of an apical
878 flagellum (f) surrounded by an actin-filled collar of microvilli (c) (13, 14). *S. rosetta*
879 produces two different colonial forms depending on environmental conditions:
880 compact, mechanically robust, roughly spherical rosette colonies (Rosette) that
881 form in the presence of specific bacterially produced Rosette Inducing Factors (RIFs;
882 (16, 17, 23, 24)), and fragile, linear chain colonies (Chain) that form during rapid cell
883 growth in the absence of RIFs (16). Both types of colonies form developmentally by
884 serial cell divisions. Single cell image adapted from (16), and rosette and chain
885 images adapted from (19). (**B**) A thin section through the equator of a rosette,
886 imaged by transmission electron microscopy, reveals the subcellular architecture of
887 a rosette. Cells in rosettes are packed close to one another around a central focus
888 with the collar complex of each cell facing outward into the environment (c=collar
889 and f=flagellum). Most cells are connected to one another by thin cytoplasmic
890 bridges (br, only two of which are visible in this section) (37), which are also
891 present in chains (16). The center of rosettes is devoid of cells but is filled with a
892 secreted extracellular matrix (e, faintly visible here as granular material), into which
893 cells extend filopodia (fi) (16, 18). All scale bars = 3 μm.

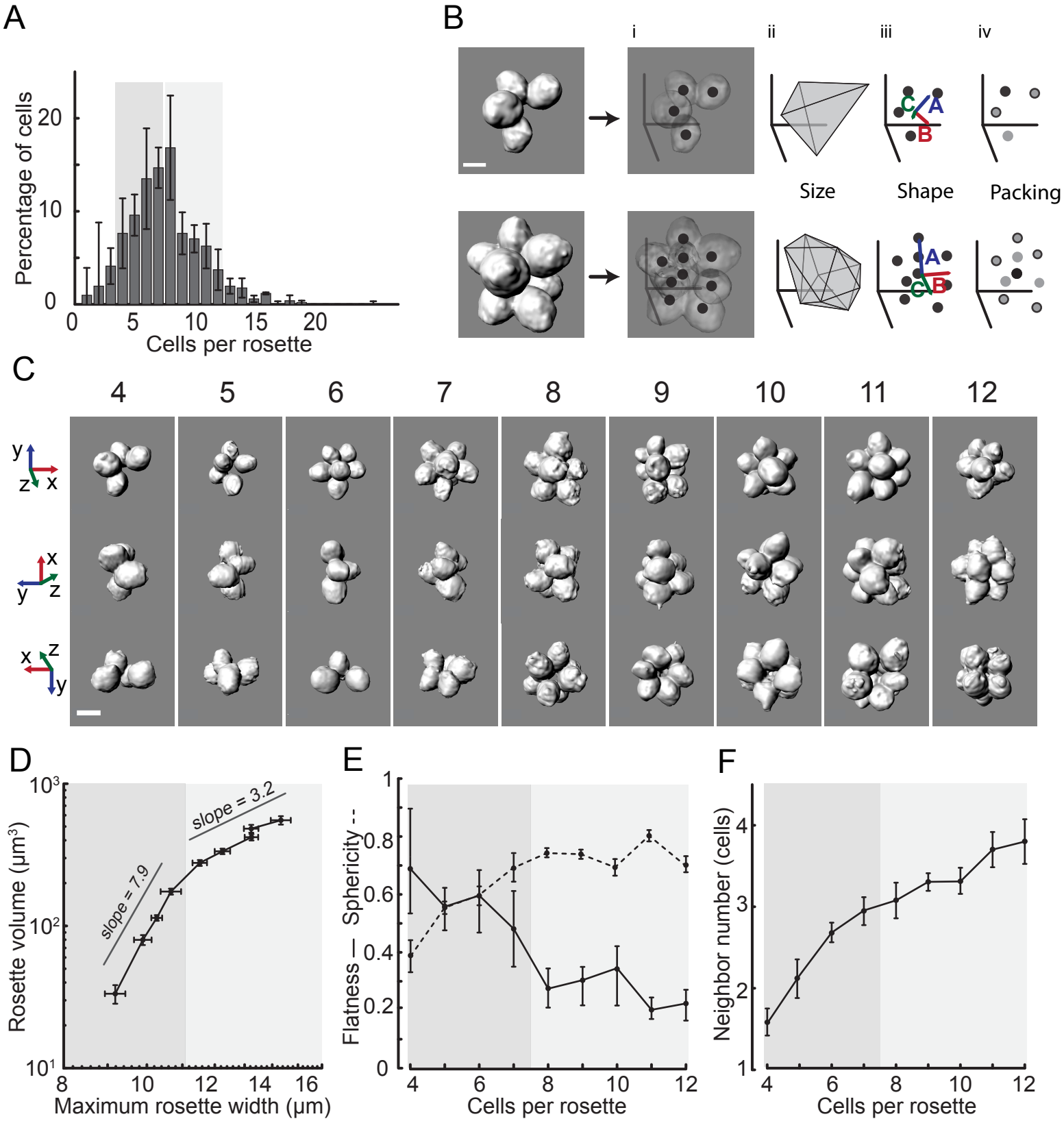

894 **Figure 2. Quantitative analysis of rosette morphology reveals that rosettes**
895 **undergo a reproducible 2D-3D growth transition**. (**A**) In cultures grown under
896 conditions of constant rosette induction, *S. rosetta* existed as unicells, doublets,
897 triplets, and rosettes containing between 4 - 25 cells (an "individual" refers to any
898 unicell or group of cells in each of these categories), with the most common rosette
899 size being 8 cells/individual. Shown is the mean percentage of total cells in a
900 population (y-axis) found in single cells, cell doublets, cell triplets, and rosettes of
901 increasing size, plotted by number of cells/rosette (x-axis). Error bars indicate
902 standard deviations from measurements obtained on three different days. N = 511.
903 (**B**) Our image analysis pipeline allowed us to quantify and compare rosette
904 morphology and is illustrated here for two representative rosettes. From left to
905 right, for each rosette, (i) cell positions were extracted from segmented images and
906 then used to determine aspects of rosette morphology including (ii) rosette size,
907 including volume (measured by generating a convex hull), (iii) shape, including
908 flatness and sphericity (the former quantified by $1 - C/B$ and the latter by $\sqrt[3]{BC/A^2}$
909 where A, B, and C are the principle axes in descending order by magnitude of a
910 principle components analysis-based ellipsoid fit of cell positions), (iv) and cell
911 packing (neighbor number determined by Voronoi tessellation(80)). (**C**)
912 Representative rosettes are shown in three roughly orthogonal views for size
913 classes ranging from four to 12 cells/rosette, with the numbers above each image
914 column indicating the number of cells/rosette. Following previous work (24), we
915 defined four cells as the smallest number of cells clearly identifiable as a rosette. (**D**)
916 Rosettes transition from an early phase of major shape change (dark grey; scaling

917 exponent ~8) to a later phase of approximately isotropic growth (light grey; scaling
918 exponent ~3), as shown by a log-log plot of rosette volume (y-axis) vs. maximum
919 rosette width (x-axis). (**E**) Rosettes transition from a relatively flat morphology
920 during the 4-6 cell stage (dark grey; mean flatness ≅ 0.5 – 0.7 and mean sphericity ≅
921 0.4 - 0.6, with flatness = 1.0 perfectly flat and sphericity = 1.0 perfectly spherical) to
922 a more spheroidal morphology during the 8-12 cell stage (light grey; mean flatness
923 ≅ 0.2 – 0.3 and mean sphericity ≅ 0.7-0.8). (**F**) Packing increases with number of
924 cells at a decreasing rate. Points on plots D-F represent mean values; error bars
925 indicate standard error of the mean. N = 100 rosettes, with at least 8 rosettes from
926 each cell-number class, pooled from three different samples. All scale bars = 3 μm.

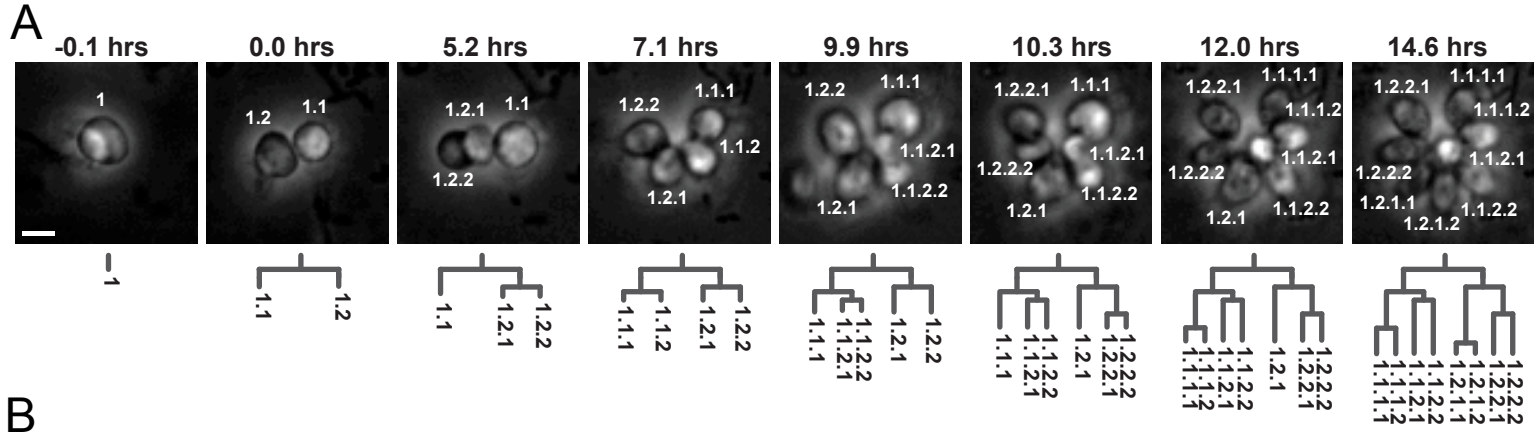

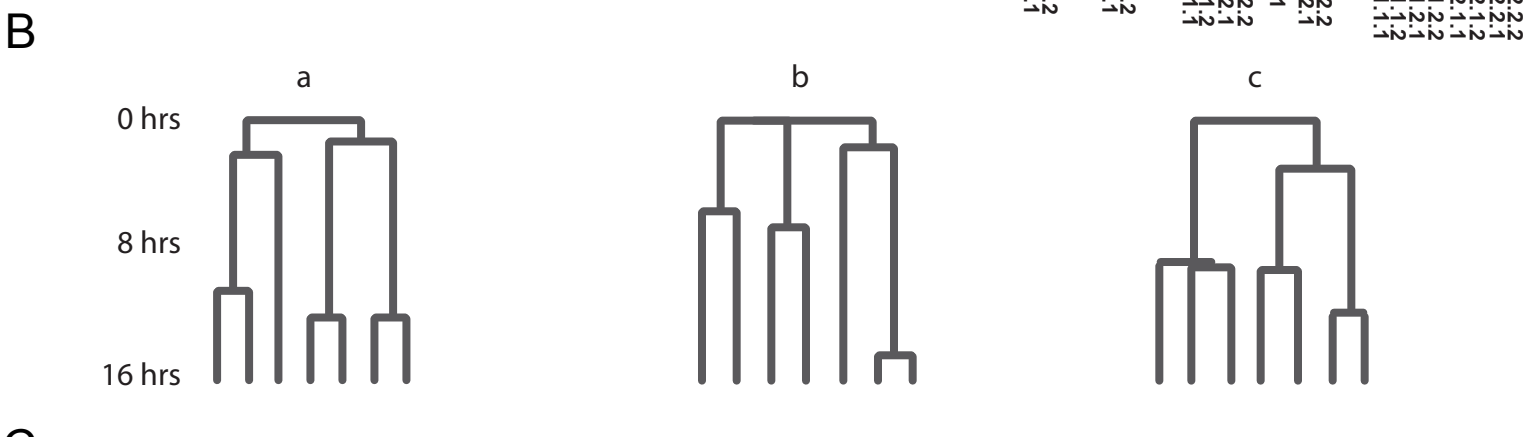

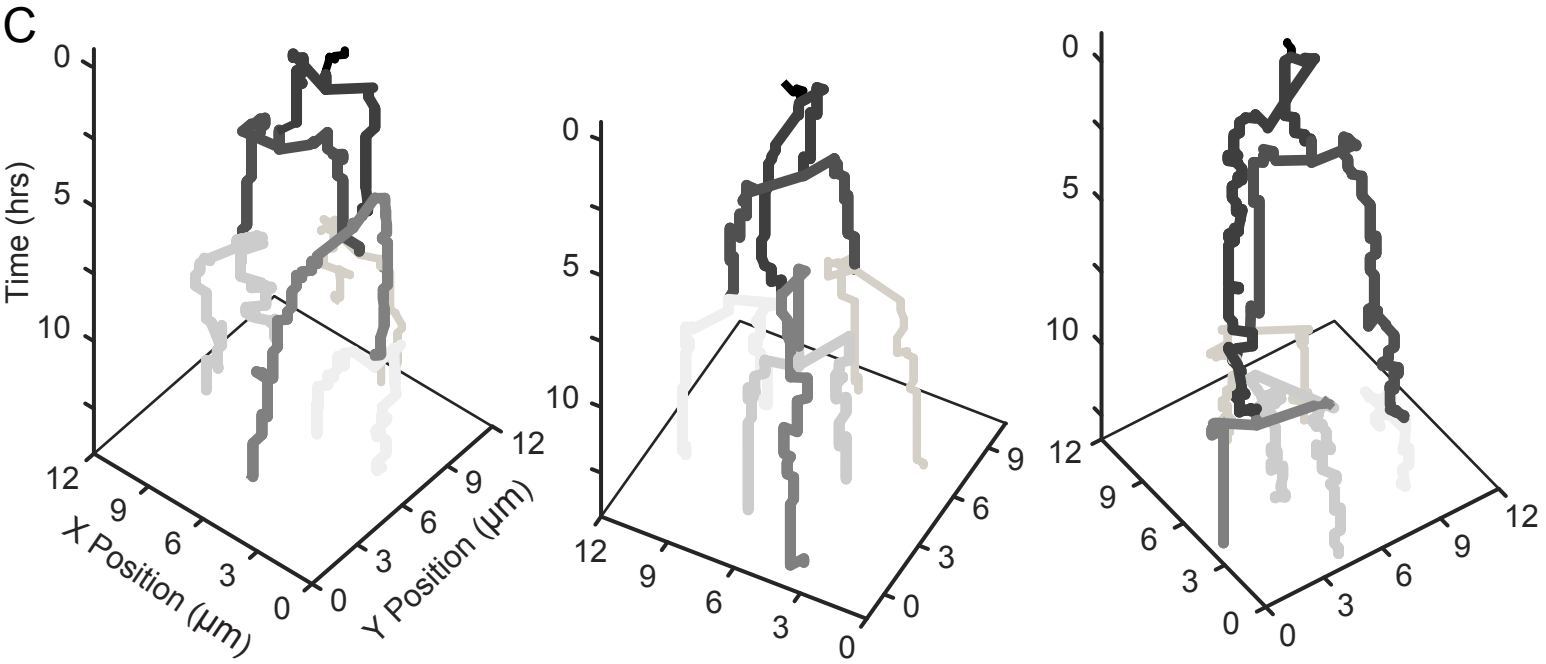

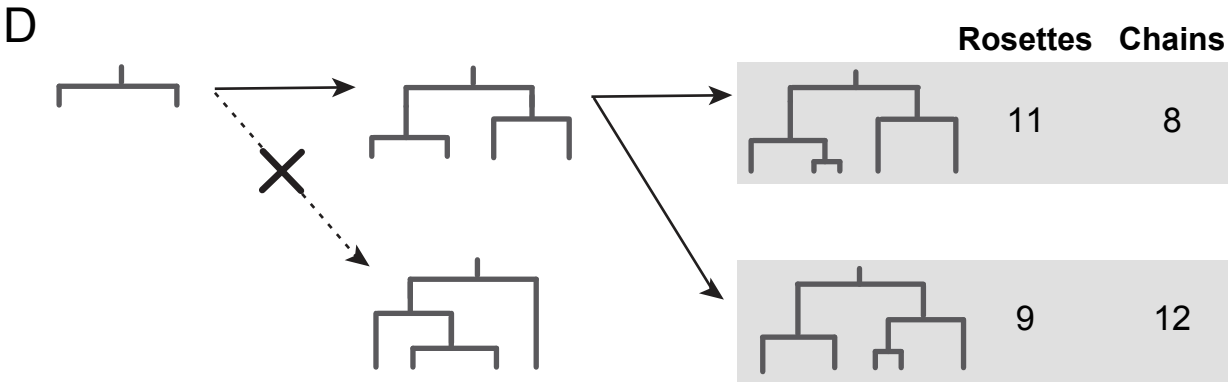

Figure 3. Stochasticity of developmental dynamics revealed by lineage analysis. (**A**) Lineage analysis for a representative rosette, imaged live by time lapse microscopy. Individual daughter cells were marked to record their relationship to their parent lineage (e.g. 1.1 and 1.2 are daughters of cell 1). Scale bar is 3 μm. (B) Representative cell lineages during rosette development illustrating differences in both the order and timing of cell divisions, with the first two on the left having the same division order but with large differences in division times, and the lineage on the right showing differences in both division order and timing. Branch lengths scale with time and are set to zero based on the first division. (**C**) Lineages a-c from (B) displayed as space-time plots illustrate cell division variability between rosettes in both space and time. Plots also demonstrate that cells remain in place after divisions, with no large rearrangements, moving apart only slightly as they grow. Colors from dark to light gray indicate the order of cell divisions. (**D**) Cell lineages that form during rosette and chain development are balanced, although the specific times of cell divisions in different lineages and different rosettes or chains can differ. In rosettes and chains, imbalanced lineage structures (i.e. with significantly different numbers of cells) were not observed at any stage. Shown here are results for four and five-cell rosettes and chains. The dashed line with an "x" indicates that this division pattern was never observed. Furthermore, this uneven branching pattern was never observed in sub-lineages of any developing chain or rosette. Data were pooled from three different rosette induction experiments (for rosettes) and three different experiments with uninduced cells (for chains).

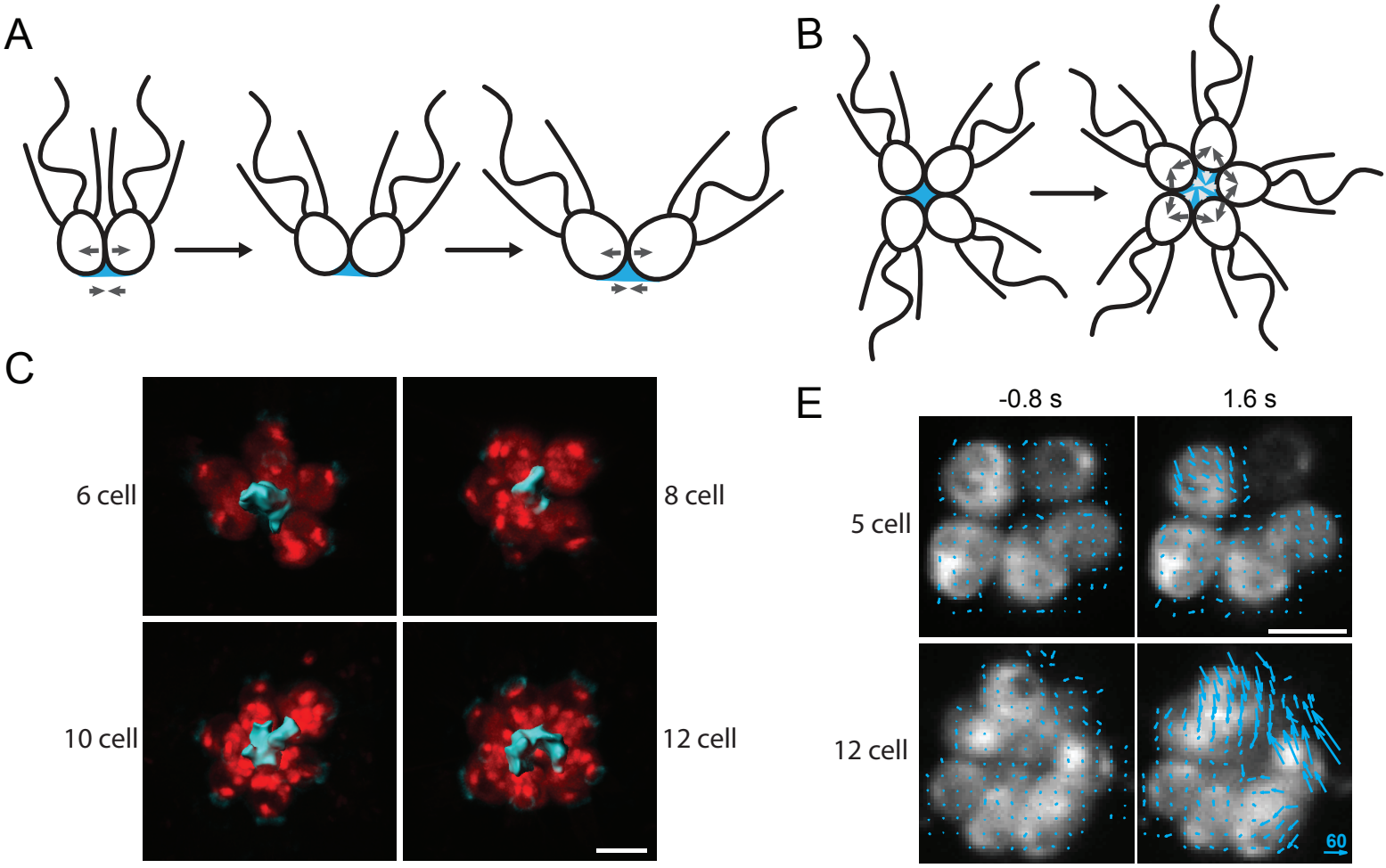

949 **Figure 4. Extracellular matrix constrains proliferating cells during rosette**
950 **morphogenesis.** (**A**-**B**) Cartoons depicting ECM constraint hypothesis. (**A**) As cells
951 grow, compressive forces exerted on neighboring cells (top set of arrows) may be
952 balanced by stress in the basally-secreted ECM (blue), which resists deformation
953 (bottom set of arrows). (**B**) If ECM is limiting, rosettes may undergo a jamming-like
954 transition and accumulate residual stress as cells continue to grow and divide. (**C**)
955 Representative images of 4 different rosettes of various sizes (of 6, 7, 8, and 10
956 cells/rosette ordered from left to right, top to bottom) with ECM tagged using
957 Jacalin. (**D**) Ratio of total ECM volume to total cell volume as a function of
958 cells/individual is maintained at a constant level over the course of rosette
959 development. Points represent mean values, and error bars are bootstrap 95%
960 confidence intervals. Data were collected from 93 rosettes pooled from two
961 experiments, with at least 5 rosettes from each size class. Image processing and
962 analysis proceeded similarly to that described in Fig. 1. (**E**) Laser ablation revealed
963 increasing stress as a function of cells/rosette. Single cells in rosettes were ablated,
964 and recoil velocities were measured by particle image velocimetry (PIV). Arrows in
965 the images indicate the direction and magnitude of the velocity of the recoil as
966 determined by PIV. Rosettes were found to always close when recoil was observed
967 (in all cases beyond the 5-cell stage). (**F**) Recoil velocities (rescaled by the length
968 scale of the average cell diameter of 5 μm and the time scale of the average division
969 time of 6 hrs.) increased with increasing cells/rosette, indicating increasing stress as
970 a function of cells/rosette (7, 39, 43). These results are consistent with the ECM
971 constraint hypothesis and inconsistent with cytoplasmic bridges or cell-cell

adhesion as the dominant factors stabilizing rosette structure. Points indicate mean values; error bars indicate standard error of the mean. Data were collected from 47 rosettes pooled from 3 different rosette inductions, with at least 4 rosettes from each size class. Scale bars = 5 μm.

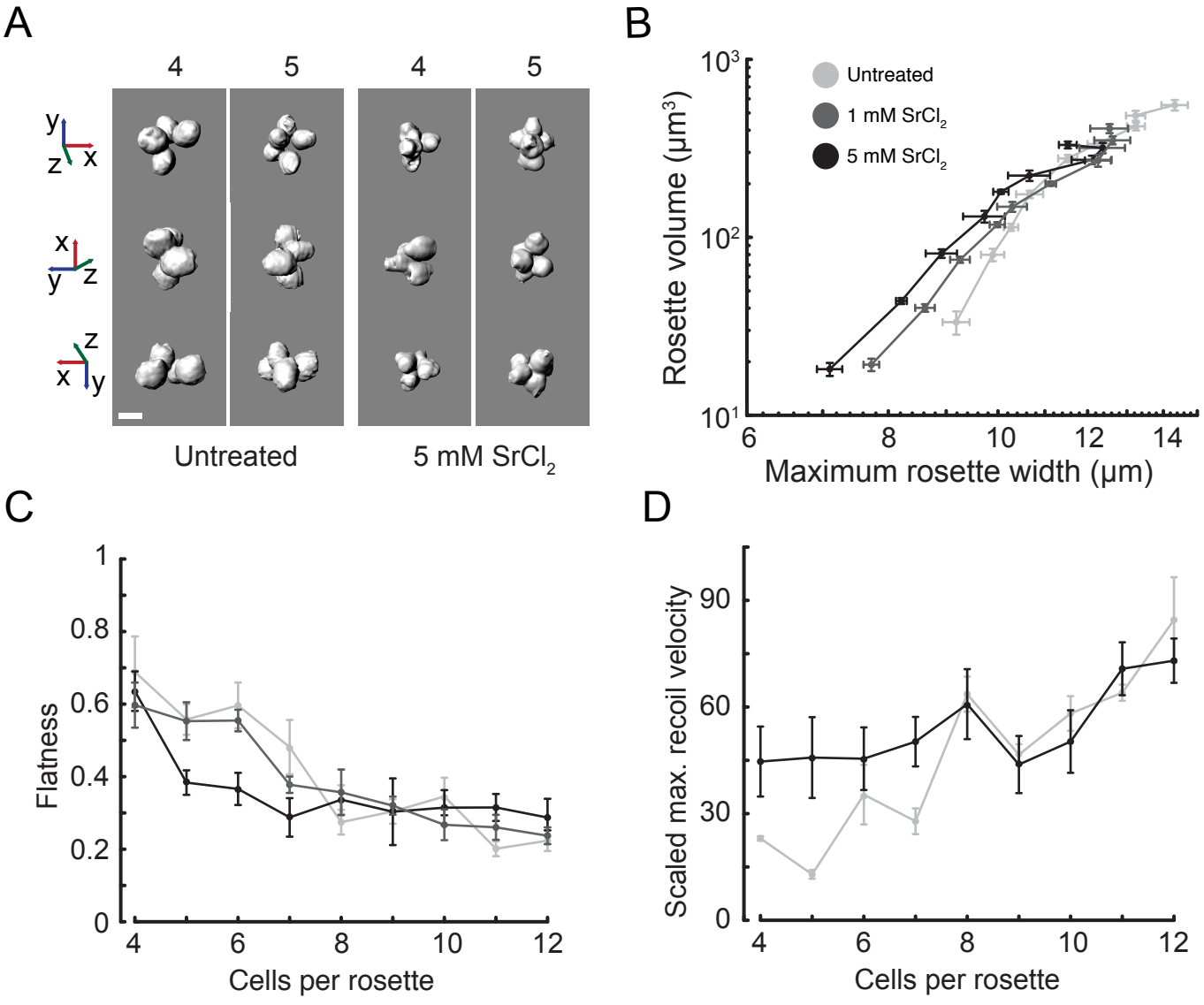

Figure 5. Material properties of the ECM affect morphogenesis, consistent with predictions of the ECM constraint hypothesis. Treatment of rosettes with $SrCl_2$, which stiffens hydrogels by increasing crosslinking density (44–48), alters rosette morphogenesis. (**A**) Representative images of untreated and $SrCl_2$-treated rosettes illustrate the change in rosette morphology. Cells were packed more tightly in $SrCl_2$ treated rosettes, leading to differences in rosette size and shape. Scale bar = 4 μm. (**B**) The scaling relationship between maximum rosette width and volume revealed that $SrCl_2$ abolished the transition to approximately isotropic growth observed in untreated rosettes. As in Fig. 2D, this is a log-log plot of rosette volume vs. maximum rosette width, with each point representing average values for a rosette cell-number class from 4-12 cells/rosette. Error bars are standard error of the mean. This analysis also revealed that rosettes became increasingly compact with increasing $SrCl_2$ concentration. (**C**) Quantification of rosette flatness (as in Fig. 1), showed that $SrCl_2$ shifts the 3D growth transition to lower cell numbers. In the case of the highest $SrCl_2$ concentration, the transition occurred by the 5-cell stage. For both (B) and (C), results were from a total of 100 rosettes pooled from 3 experiments, with at least 8 rosettes for each size class for both $SrCl_2$ concentrations. (**D**) Relative residual stress, as measured by maximum initial recoil velocity (rescaled, as in 4E, F, by the length scale of the average cell diameter of 5 μm and the time scale of the average division time of 6 hrs.) after laser ablation of single cells (as in figure 4E, F), increased in rosettes of 4-7 cells under 5mM $SrCl_2$ treatment compared to untreated rosettes. These data demonstrate that increased residual stress is correlated with altered cell packing and hence, altered rosette morphology. Points represent means

and error bars represent standard error of the mean from 41 total measurements pooled from two experiments, with at least 4 rosettes from each size class.

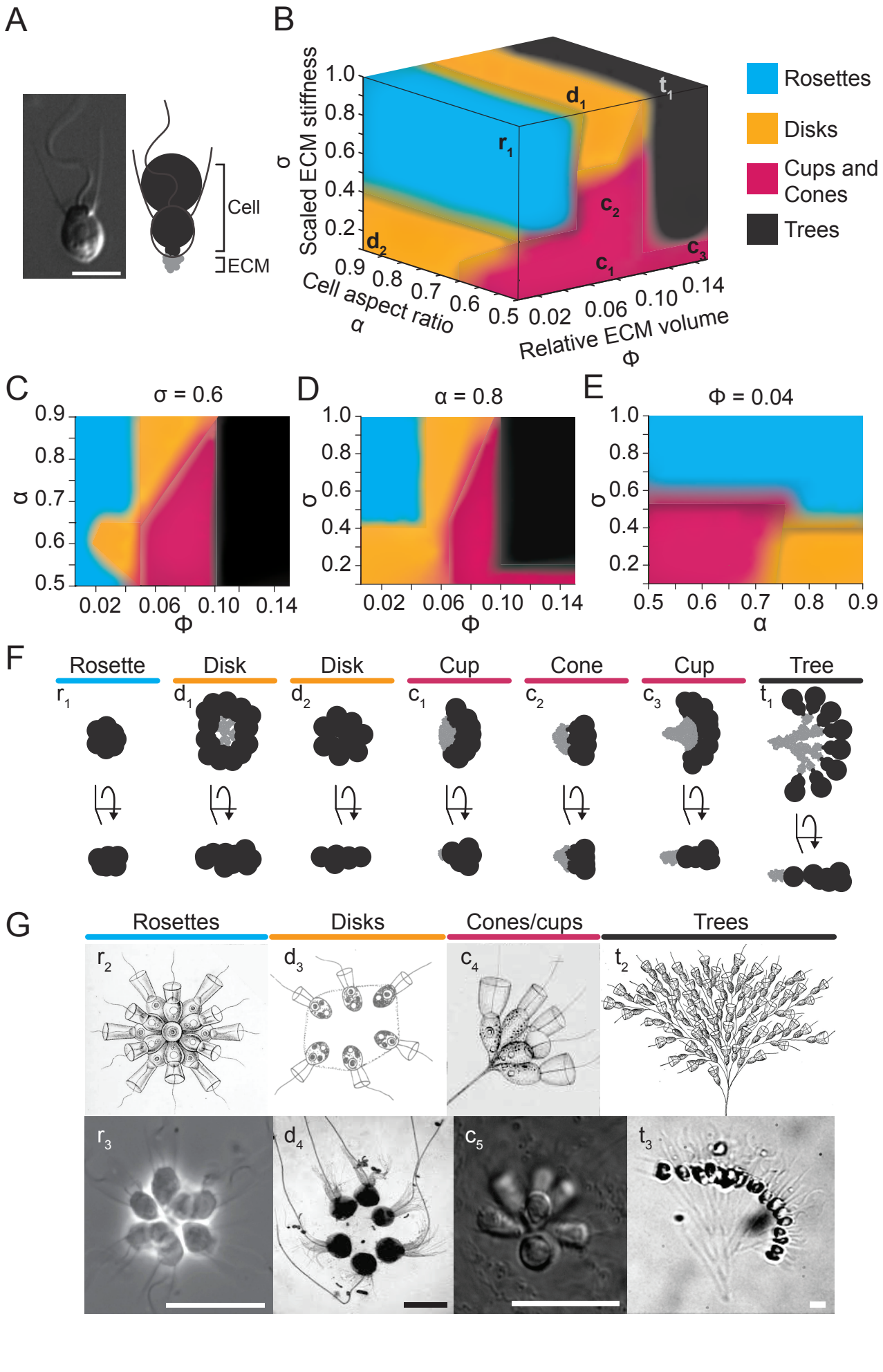

Figure 6. A simple model shows that amount of ECM, cell shape (aspect ratio), and ECM stiffness tune multicellular morphogenesis. The model incorporates simple cellular and physical interactions, including ECM secretion and cell division, cell-cell steric interactions, and ECM adhesion. Three main parameters describe the system: cell aspect ratio, α, scaled ECM stiffness, σ, and relative ECM volume, ϕ. (**A**) An image of a choanoflagellate (adapted from (16)) next to a simulation snapshot to illustrate how cell geometry is modeled by three linked spheres (black) and ECM is modeled by small spheres (grey) secreted at the basal pole of cells. In the model, cells interact sterically with one another, and ECM spheres have adhesive interactions with one another and with basal cell particles. Scale bar = 5 μm. (**B**) The morphospace of ECM-based colonial morphologies generated by simulations can be broken into four regions: rosettes, disks, cones/cups, and trees as denoted by colors as indicated in the legend. The lower-case letters indicate approximately the point in the morphospace occupied by the corresponding simulated colony in panel F. (**C**-**E**) Orthogonal planes through the displayed morphospace, with the parameter of fixed value noted above each plot, illustrate how changing two parameters while keeping the third fixed affects morphology. Colors indicate morphological classification as in panel B. (**C**) Scaled ECM stiffness is constant (σ=0.6). (**D**) Cell aspect ratio is constant (α=0.8). (**E**) Relative ECM volume is constant (ϕ=0.04). (**F**) Representative simulated colonies for each of the regions are displayed in two orthogonal views ($\mathbf{r_1}$=rosette with α=0.7, σ=0.8, and ϕ=0.04; $\mathbf{d_1}$=disk with α=0.75σ=0.85, and ϕ=0.075; $\mathbf{d_2}$=disk with α=0.8, σ=0.15, and ϕ=0.02; $\mathbf{c_1}$=cone with α=0.55, σ=0.5, and relative ECM volume=0.08; $\mathbf{c_2}$=cup with α=0.6, σ=0.2, and ϕ=0.09; $\mathbf{c_3}$=cup with α=0.9, σ=0.12, and

ϕ=0.13; and $\mathbf{t_1}$=tree with α=0.65, σ=0.9, and ϕ=0.12). Note that d_2 and c_3 represent extreme ends of the morphospace to better illustrate, along with the other representative simulation snapshots, how changing the model parameters affects the simulated morphologies. (**G**) Simulated colonial morphologies are reminiscent of morphologies of colonial choanoflagellates found in nature. ($\mathbf{r_2}$) *Codonosiga botrytis* (86). ($\mathbf{r_3}$) *Salpingoeca rosetta* (87). ($\mathbf{d_3}$) *Proterospongia haeckelii* (88) (Ertl after Lackey). ($\mathbf{d_4}$) *Salpingoeca amphoridium* (10). ($\mathbf{c_4}$) *Codosiga umbellata* (53). ($\mathbf{c_5}$) Uncharacterized environmental isolate collected from Mono Lake by Daniel Richter, *Salpingoeca sp*. ($\mathbf{t_2}$) *Codosiga cymosa* (52) (Calkins after Kent). ($\mathbf{t_3}$) Uncharacterized environmental isolate from a tide pool in Curaçao, *Salpingoeca sp*. Scale bars = 10 μm.